Effect of input perturbation on the performance and wake dynamics of aquatic propulsion in heaving flexible foils

Andrea M. Lehn

Department of Mechanical Engineering, Massachusetts Institute of Technology, 77 Massachusetts Ave, Cambridge, MA 02139, USA

Patrick J. M. Thornycroft and George V. Lauder

Department of Organismic and Evolutionary Biology, Harvard University, 26 Oxford St., Cambridge, MA 02138, USA

Megan C. Leftwich[*]

Department of Mechanical and Aerospace Engineering, The George Washington University, 800 22nd St., NW Washington, DC 20052, USA

In this paper we consider the effects of adding high-frequency, low-amplitude perturbations to a smooth sinusoidal base input signal for a heaving panel in a closed loop flow tank. Specifically, 0.1 cm amplitude sinusoidal perturbation waves with frequency f_p ranging from 0.5 to 13.0 Hz are added to 1 cm heave sinusoids with base frequencies, f_b, ranging from 0.5 to 3.0 Hz. Two thin foils with different flexural stiffness are heaved with the combined input signals in addition to both the high-heave and low-heave signals independently. In all cases, the foils are heaved in a recirculating water channel with an incoming velocity of $V_x = 10$ cm/s and a Reynolds number based on the chord length of Re = 17 300. Results demonstrate that perturbations increase the net axial force, in the streamwise direction, in most cases tested (with the exception of some poor performing flexible foil cases). Most significantly, for a base frequency of 1 Hz, perturbations at 9 Hz result in a 780.7% increase in net streamwise force production. Generally, the higher the perturbation frequency, f_p the more axial force generated. However, for the stiffer foil, a clear peak in net force exists at $f_p = 9$ Hz, regardless of the base frequency. For the stiffer foil, swimming efficiency at a 1 Hz flapping frequency is increased dramatically with the addition of a perturbation, with reduced efficiency increases at higher flapping frequencies. Likewise, for the flexible foil, swimming efficiency gains are greatest at the lower flapping frequencies. Perturbations alter the wake structure by increasing the vorticity magnitude and increasing the vortex shedding frequency; i.e., more, stronger vortices are produced in each flapping cycle.

I. INTRODUCTION

The remarkable locomotor capability of fishes, the result of over 500 million years of evolution, has stimulated a wide variety of research on aquatic propulsion. Fish excel at both steady swimming and maneuvering and produce wavelike motions of their fins and body to generate thrust. Both fin and body deformation during locomotion can involve the production of complex waveforms, and flexibility is a key design feature of fish fins and body. It is thus not surprising that fish locomotion has been used as inspiration for understanding the fundamental physics of unsteady motion and to inspire novel designs for propulsive underwater systems [1–4].

---
[*]mleftwich@gwu.edu

Experiments on the kinematics and hydrodynamics of freely swimming fishes have involved measuring body and fin waveforms and correlating these deformations with wake flow patterns. The influence of flexibility on the hydrodynamics of swimming has been investigated for a range of experimental and computational systems [5–8]. One investigative method is to use reduced-order physical models, such as pitching and/or heaving hydrofoils [9–12]. Typically, a smooth, periodic, input signal is used to control the leading edge of foil motion in experiments that explore fundamental factors (aspect ratio [13], shape [14], flexibility [15], etc.) in swimming performance.

However, there are two reasons to believe that use of simple sinusoidal input motions can be improved, and that such relatively simple control signals do not accurately represent the mechanism by which motor output is generated in many biological systems. First, prior research on patterns of fin and body deformation in freely swimming fishes has demonstrated that complex waveforms are generated during propulsion, and that kinematic deformation may involve multiple waves of different frequency and amplitude on the fins [6,16]. Body waveforms may also possess a number of dominant frequency components [17,18].

Second, the generation of the control signal in biological locomotor systems typically involves the *combination* of a base output signal and a modulatory signal produced by sensory inputs of various kinds [19–22]. The control of biological locomotion thus involves neuromechanical interactions in which the final output control signal has resulted from multiple inputs that include modulation of a pattern-generated base program. Taking inspiration from this recent research in the neuromechanics of locomotion, the purpose of this paper is to demonstrate that it is profitable to investigate more complex control signals for reduced-order physical models and begin to move beyond single sinusoidal inputs for swimming flexible panels. To our knowledge, previous studies of locomotion using physical models have not used more complex driving waveforms that are likely to reflect at least some of the complexity of biological inputs to the locomotor system. We believe that study of more complex input waveforms to locomotor structures and their effect on force production and swimming efficiency represents an intriguing area for research in aquatic propulsion and can lead to unexpected effects on the performance and efficiency of swimming systems. Thus, we focus in this paper on the impact of perturbed input motions on swimming performance in a simple foil model locomotor system.

Previous research using simple physical models to understand aquatic propulsion has devoted considerable attention to wake structures produced during locomotion. Typically, wakes are characterized by the nomenclature of Williamson and Roshko [23]. They found wake structures downstream of an oscillating cylinder were formed from vortices shedding from the body every half cycle, in one of two ways: either as a single vortex (2S) or as a same sign pair (2P). In the 2S wake, a starting-stopping vortex is created when the cylinder reaches the maximum amplitude of its oscillation and changes direction. That vortex moves into the wake as a single entity and is convected downstream. One half cycle later, as the cylinder changes direction again, it creates a starting-stopping vortex with the opposite direction of rotation, shed as before. If this cylinder forms a classic von Kármán vortex street, it produces drag. However, if the unsteady oscillations produce a wake structure that is a reverse von Kármán street, it will produce a positive streamwise force. In a reverse von Kármán street, the vortices induce a velocity in the same direction as the mean flow. A third 2S scenario occurs when the body drag of the cylinder is matched by the thrust produced by unsteady motion. In this case, the 2S structure will produce no net thrust. Starting-stopping vortices, however, do not always shed as one distinct entity. When this happens, we see a common variation of the 2S structure known as 2P. In 2P wakes, the starting-stopping vortex is split into two distinct vortices (the primary and secondary vortices) with individual cores. The primary vortex stays on the side of the wake in which it is shed, while the secondary vortex is convected to the opposite side of the wake, forming a pair with the primary vortex from the next cycle.

Although biological oscillators are ubiquitous in nature, how these systems respond to small, destabilizing perturbations is relatively unclear, and the effect of more complex input oscillations on locomotor thrust, efficiency, and wake structure is unknown. Hover *et al.* [24] investigated the effect of input shape with relation to the relative angle of attack of a flapping foil. They found

TABLE I. Foil parameters.

Foil	E (GPa)	δ (mm)	EI (Nm^2)
Flexible	1.9	0.1	3.3×10^{-5}
Stiffer	4.5	0.5	9.9×10^{-4}

that the input signal can significantly effect performance; a cosine wave is most efficient while the sawtooth produces the most force. While Hover *et al.* and others did consider the shape of the input with regard to swimming performance [24–27], they did not consider the effect of a single, small perturbation on a smooth signal.

Sensory and mechanical perturbations to oscillatory motion may be important for quantifying the underlying neuromechanical control mechanisms that enable locomotion in animals [28]. Intrinsic neuromuscular variability, complex changes in flexural stiffness along the body, and complex fluid-structure interactions in biological materials make input-output mapping difficult for systems such as undulating swimmers. In this study we focus on the effect of input perturbations on streamwise force generation and swimming efficiency of simple heaving panels of two flexural stiffnesses and on characterizing wake structures produced as input perturbations change. These data show how a simple model system in which input perturbations can be systematically added to a control signal can be used to understand the effects of biological oscillatory inputs and to improve current control systems for unsteady propulsors.

II. METHODS

We moved two flexible foils (or panels) of different stiffness over a range of input motions by oscillating the leading edge of the panel in a heave motion following the protocols and test flow tank used in our previous work on swimming flexible panels [29–32]. The two plastic foils were cut from a collection of plastic shimstock (ARTUS Corp.). The relatively flexible foil (tan color in the shimstock collection) has a stiffness of $EI = 3.3 \times 10^{-5}$ Nm^2, and the stiffer foil (yellow color in the shimstock collection) a stiffness of $EI = 9.9 \times 10^{-4}$ Nm^2 (see Table I), where EI is defined as $EI = Es\delta^3[12(1 - \nu^2)]$ where E is the modulus of elasticity of the foil material, s is the foil span, δ is the foil thickness, and ν is Poisson ratio, taken to be 0.3 for both foils. The 5:3 aspect ratio panels have chord lengths (in the direction of flow) of 18 cm and span widths of 10.8 cm. Foils were effectively two-dimensional, being thin relative to their length and chord, with foil thickness equal to $\delta = 0.1$ mm and $\delta = 0.5$ mm for the flexible and stiffer materials, respectively. The two foils were chosen (both shape and stiffness) because of the availability of comparable data for smooth signals. See Fig. 1 for a schematic of the foil shape. A constant flow speed of $U = 10$ cm/s was used for each experiment (this is approximately the free swimming speed of the stiffer panel heaving about its leading edge at 1 Hz with a 1 cm heave amplitude). Reynolds number (Re $= \frac{UL\rho}{\mu}$, where ρ and μ are the fluid density and viscosity, respectively) of each experiment was 17 300.

A. Input perturbation

We performed both base signal and perturbation signal frequency sweeps: base signals had 10 mm heave amplitude and frequencies ranging from 0.5 to 3.0 Hz in 0.25 Hz increments. Perturbation signals had 1 mm heave amplitude and frequencies ranging from 0.5 to 13 Hz. A smooth sinusoid ("base" signal) is overlaid with high-frequency, low-amplitude perturbations as the input signal for a heaving panel in a recirculating flow tank. Specifically, the perturbed inputs were generated by adding a 1 cm heave amplitude ($A = 1$ cm) base sinusoid with frequencies (f_b) ranging from 0.5 to 3.0 Hz, to a 0.1 cm heave perturbation signal with frequencies (f_p) ranging from 0.5 to 13 Hz. That is, a smooth base signal is overlaid with an oscillatory, low-heave amplitude but higher frequency
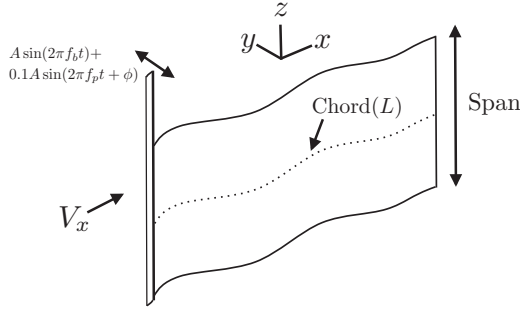
FIG. 1. A diagram showing chord and span of the heaved foil. The function that controls heave motion of the leading edge is shown in the upper left. Note that the base frequency, f_b ranges from 0.5 to 3.0 Hz, and f_p is the perturbation frequency and ranges from 0 (no perturbation) to 13 Hz. V_x is the incoming flow velocity of 10 cm/s for all runs.

"perturbation" (see Fig. 2) to generate a driving signal, $I(t)$, according to the following equation:

$$I(t) = A \sin(2\pi f_b t) + 0.1A \sin(2\pi f_p t + \phi), \tag{1}$$

where in addition to already defined variables, t is time and ϕ is a phase shift between the two signals used to avoid overloading the driving motor. This value was set to $\phi = \pi/2$. It is noted that, for high values of f_p, the velocity of the perturbation $(0.1A * f_p)$ is the same order as the velocity of the base signal.

A 1 cm heave was chosen as the base input to allow comparison to previous work [15]. For simplicity, we considered only pure heave (i.e., no pitch). The range of frequencies chosen (for both
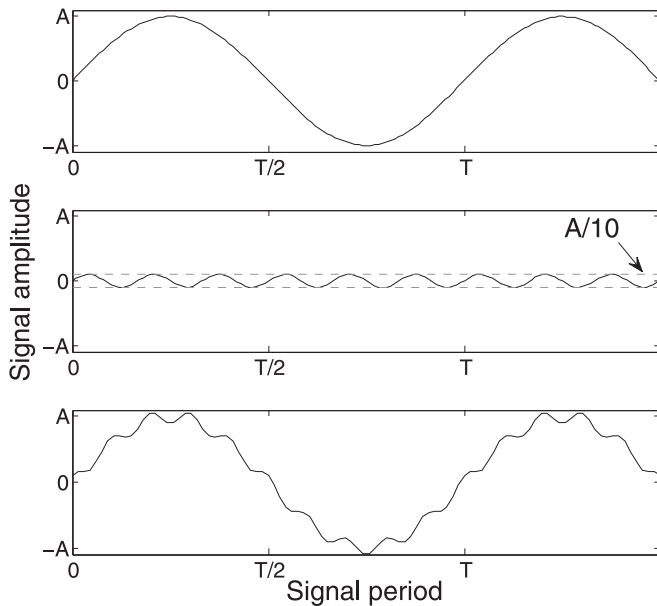

FIG. 2. The base, smooth, input is a sinusoid with amplitude A and period T shown in the top panel. An example perturbation signal is shown in the middle panel. This example has a period of $T/9$ and an amplitude of $A/10$. In the experiments, the perturbation frequency ranged, f_p, from 1–25 times the input frequency, f_b. The experiments were carried out with the combined "perturbed signal" shown in the bottom panel, as well as separately with the smooth input signal and the higher frequency perturbation alone.
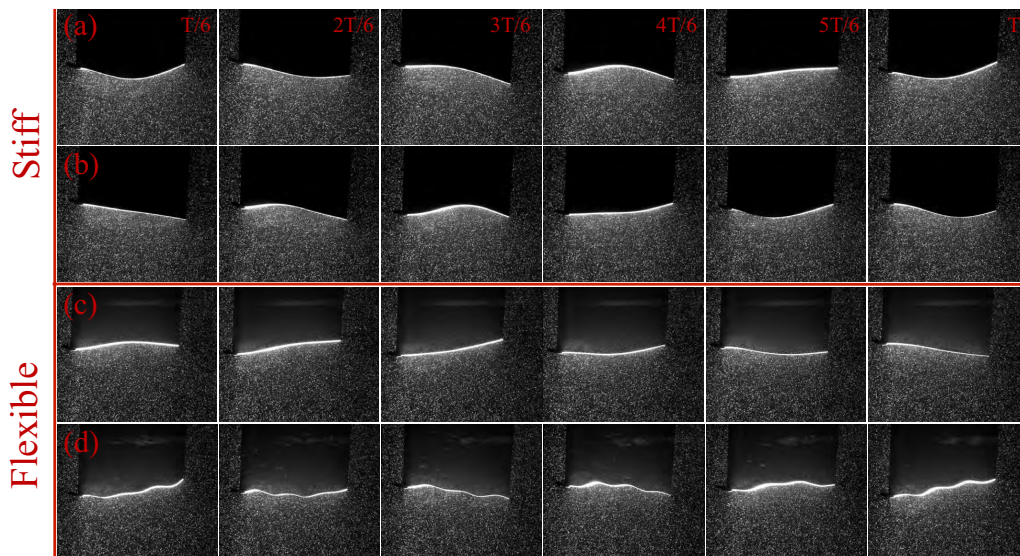
FIG. 3. The top panels (above the red line) show the stiffer foil ($EI = 9.9 \times 10^{-4}$) with a smooth 1 cm heave input with a base frequency of $f_b = 3$ Hz and no perturbation (a) and the same base frequency with a 0.1 cm perturbation at a frequency of $f_p = 9$ Hz (b). Below the red line, the panels show the flexible foil ($EI = 3.3 \times 10^{-5}$) undulating with a smooth input, $f_b = 0.5$ Hz base frequency, 1 cm heave amplitude (c) and the same foil heaving with a perturbed input generated by adding a $f_p = 12.5$ Hz, 0.1 cm heave amplitude perturbation to the 0.5 Hz smooth motion (d). One cycle of the base signal is shown in each row, and the images are taken from raw PIV data.

f_b and f_p) provides a large parameter space, while limiting us to the general range of midsized fish motions. For this study, only smooth signals were considered (as opposed to those generated by band-limited noise signals), although it is expected that more complicated perturbations will be explored in the future.

Both were moved in three ways: (1) using the high-heave base frequencies only, (2) using the low-heave and high-frequency input perturbation only, and (3) with the combined signals referred to as a "perturbed input" $I(t)$. One cycle of motion for the flexible foil is shown for both a smooth, unperturbed signal and a perturbed input in Fig. 3.

B. Heaving foil apparatus

During experimental trials, foils were anchored above the flowtank and secured to a thin carbon fiber rod at the leading edge. The foil was submerged in the recirculating flow tank. A stepper motor on the other end of the rod, above the flow tank, heaved the foil with a user specified input motion. The flow speed was prescribed by the user. The motor and flow speed were controlled by LabVIEW graphical user interfaces (GUIs). An ATI Nano-17 six-axis force/torque sensor (ATI Inc., Nano-17 SI-50-0.5) was attached to the foil shaft to allow three force and torque measurements in an xyz coordinate system; see Fig. 1. The x direction is aimed downstream, z points vertically up the shaft, and y points in the direction of heave motion (normal to flow).

Foils were attached to a carbon fiber supporting element (Fig. 1) that bolts to the leading foil edge and attaches to the ATI transducer above. A motor mounted above the flow tank enabled lateral motion of the foil in normal to free-stream flow, and a LabVIEW program was used to implement the control protocol. Position data of the leading edge were obtained from an encoder on the heave motor throughout each experimental trial. LabVIEW programs were used to collect the force and

torque data on the supporting shaft, and then stored locally for processing. Data were processed and plotted using iPython.

C. Measurements

We measured both the forces generated by the heaving panel and, for some cases, the resulting flow field.

1. Streamwise force and efficiency

Force and torque data from the ATI transducer were used to calculate both the mean axial (streamwise) force coefficient and efficiency for each tested case as in Refs. [15,31–33]. The mean force coefficient, C_F, for each trial was calculated as 2 times the average streamwise force per cycle (F_x mean) divided by fluid density times swimming velocity squared, times the foil surface area (note that F_x is the measured force in the streamwise direction, i.e., the propulsive force minus the drag of the foil). Thus,

$$C_F = \frac{F_x}{1/2 \rho A V_x^2}.$$ (2)

Swimming efficiency was calculated as the force coefficient divided by the power coefficient [33]:

$$\eta = \frac{F_x V_x}{P}.$$ (3)

Power, P, was calculated as force (F_y, measured directly) times the velocity of heave motion, and mean values of each over a flapping cycle allowed calculation of the power coefficient. Foils were moved in heave only at the leading edge, and no rotational (pitch) motions were introduced.

2. Flow visualization

Wake analysis for selected cases was performed using particle image velocimetry (PIV) as in Refs. [15,30,32]. A Coherent 10 W continuous-wave argon-ion laser illuminated small plastic particles (10–25 μm) added to the flow tank water. Movement of particles near the flapping foil surface and in the wake during a series of two or three flapping cycles was visualized using Photron PCI-1024 high-speed cameras with a resolution of 1024×1024 pixels operating at 1000 fps. Fluid velocity and vorticity fields were calculated using DaVis software (v. 8.1.3, LaVision Inc.). A LabVIEW trigger pulse allowed simultaneous acquisition of force and torque measurements during each trial.

III. RESULTS

By measuring both the forces generated by, and the flow fields surrounding, two heaving foils of different flexibility, a complete picture of a heaving foil with a perturbed input begins to emerge. In this section we present force, efficiency, and velocity data for the 132 different $I(t)$ inputs tested.

A. Force measurements

The force coefficient [Eq. (2)] was measured for two foils each with 11 base frequencies and two to 13 perturbation frequencies, resulting in 132 total flapping inputs. The streamwise force, F_x, was measured directly (along with the lift, lateral forces, and associated torques) and is the total thrust for one cycle averaged over two cycles, as described in Sec. II C 1. ρ is the density of water, $A = 194.4$ cm^2 is the surface area of the panel, and $V_x = 10$ cm/s is the incoming flow velocity. The quantity $1/2 \rho A V_x^2$ is constant for all cases and equal to 0.0972 N. In Fig. 4, 132 axial force values are plotted. For every case, the presence of perturbation on the input heave signal increased the streamwise force produced by the foil. Note that Fig. 4 is presented in dimensional form, because
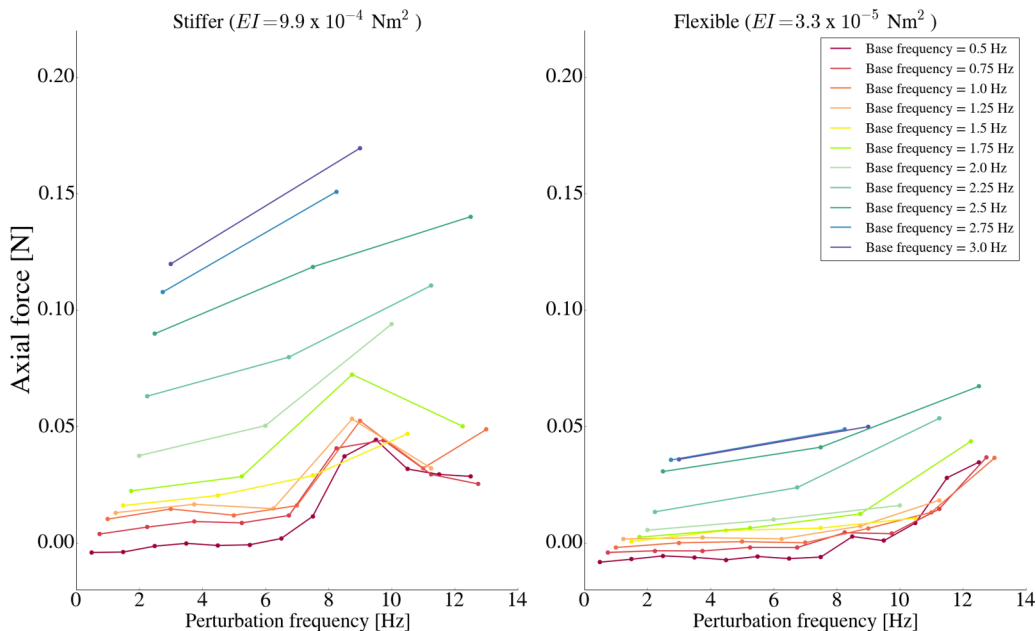
FIG. 4. The axial force, F_x, is plotted against perturbation frequency, f_p, for both the stiffer panel (left) and the flexible panel (right). All 11 base frequencies, f_b, are shown for both panels. Note that applying a perturbation always increases F_x for every case tested, and, for the stiffer foil, a distinct peak in performance exists around $f_p = 7 - 9$ Hz.

the peak in performance occurs at the dimensional perturbation frequency of $f_p = 9$ Hz for the stiffer foil, as discussed in Sec. IV.

For the stiffer foil, shown in the left side of Fig. 4, a peak in performance exists when a perturbation frequency of $f_p = 7$–9 Hz is applied to the base frequency, regardless of the value of f_b. This observation is clearly true for base frequencies up to 2 Hz. When f_b is above 2 Hz, mechanical limitations of the driving motor prevent the collection of enough data to confirm the existence and location of this peak. It is unclear in the present study if this is related to a mechanical resonance of the foil [15,34]. However, the reliability of its location, at approximately 9 Hz, suggests this may be true. The lack of a peak in the right panel of Fig. 4 may be a consequence of the more flexible foil having a mechanical resonance at a higher frequency.

For the flexible panel, the streamwise force value was still increasing when the highest f_p was tested ($f_p = 13$). It is possible that a peak similar to that seen on the stiffer foil exists at a higher perturbation frequency but could not be reached because of the physical limitations of the motors. However, the addition of the perturbation can greatly increase the forward force production of these panels. For example, the flexible foil with a 1 cm sinusoidal heave at $1/2$ Hz has a $F_x = -0.037$ N. The negative sign indicates that the free swimming speed would be less than the applied incoming velocity $V_x = 10$ cm/s. The coefficient of force slowly increases, but remains negative, until $f_p = 8.5$ Hz, when it reaches 0.003 N. By the point that a 12.5 Hz perturbation is applied, $F_x = 0.034$ N, indicating a net positive streamwise force (the free swimming speed would be greater than V_x), and demonstrating about an 800% increase in force production through the application of a high-frequency, low-amplitude perturbation. For the stiffer foil with no perturbation added at a heave frequency of 1 Hz, the axial force is near zero, indicating that the foil is self-propelling (Fig. 4).

If we consider a few select cases, specifically base frequencies of $f_b = 1$, 2, and 3 Hz with the associated perturbations, we can more easily compare the performance of the stiffer and flexible foils (see Fig. 5). While the flexible foil always produces less force than the stiffer one, there are some combinations of base and perturbation frequencies in which its performance is nearly as strong. For
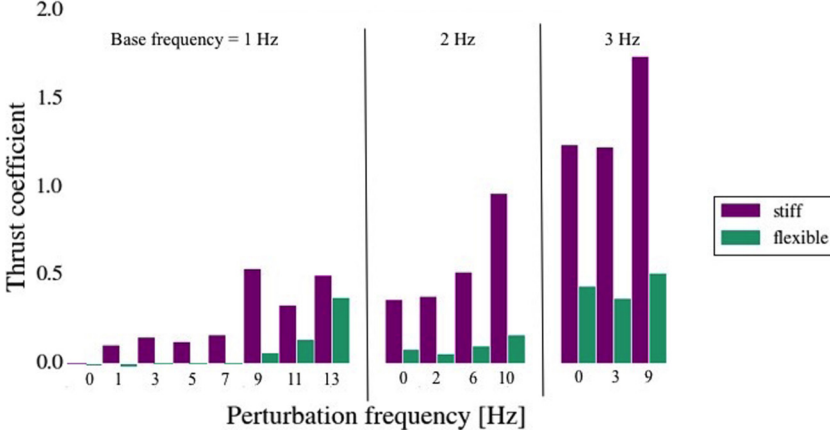
FIG. 5. The axial force ($C_F = \frac{F_x}{1/2\rho A V_x^2}$) is plotted for both the stiffer (purple, $EI = 9.9 \times 10^{-4}$) and flexible (green, $EI = 3.3 \times 10^{-5}$) foils for base frequencies of $f_b = 1$, 2, and 3 Hz and all associated perturbation frequencies.

example, when $f_b = 1$ Hz and $f_p = 13$ Hz, the performance of the flexible foil is still improving, while the stiffer foil has peaked. Note that for some cases in the left panel of Fig. 5, some of the values for C_F are very small: so small that the value registers as zero on this scale, indicating that the panel is approximately at its free swimming condition. Additionally, recall that when $f_b = 1$ Hz, the flexible foil produces negative or zero streamwise force at this V_x until f_p is above 9 Hz.

As mentioned above, we did measure the axial force of the foils with the perturbation input only, i.e., only a single sinusoid with heave amplitude of 0.1 cm. In all of the cases, the perturbation input alone, measured at the same Reynolds number ($V_x = 10$ cm/s), was drag producing. The measured force, F_x, was negative. Thus, these results, that the streamwise force increases when a perturbation is added to a base signal, are not simply the result of adding the effects of the two separate signals. That would cause a decrease in force production with perturbation, the opposite of what is seen. However, given the nonlinear nature of the Navier-Stokes equations, it is not expected that we could simply add the solutions to the two inputs measured separately to achieve the solution to the combined input.

The force coefficient tends to increase with increasing perturbation frequency, and it may not come at the cost of propulsive efficiency, η. Figure 6 shows the efficiency for the same cases as in Fig. 5. We define propulsive efficiency for thrust producing conditions, following Ref. [33], as the thrust coefficient divided by the power coefficient [Eq. (3)]. We note that when the velocity, V_x, is fixed, as it is in this study, there is the potential for negative streamwise force, as seen in this study. In those cases, propulsive efficiency will be negative and, thus, is not particularly meaningful. However, we are choosing to present those cases as they highlight the improvement in performance that perturbations can cause. Additionally, a C_F of zero (indicating steady swimming) will have an efficiency of zero regardless of the power input. Finally, unlike force coefficients [Eq. (2)], where the scaling factor $1/2\rho A V_x^2$ is a constant across cases, the denominator of Eq. (3) differs as the power to the motor P is not constant and is measured for each $I(t)$ tested.

For the stiffer foil with a base frequency of $f_b = 1$ Hz, there is an initial dramatic jump in efficiency when a perturbation is added, although the increase in C_F is comparatively modest. As f_p is increased, the efficiency remains higher than for the base frequency alone, but it always decreases below the value of the previous f_p. For higher base frequencies, $f_b = 2$ Hz and $f_b = 3$ Hz, the initial increase in efficiency is more modest (40.2% and 18.0%, respectively). The efficiency then decreases modestly as the perturbation frequency is increased.

The propulsive efficiency is more constant for the flexible foil, neglecting the somewhat unphysical, negative propulsive efficiencies when the foil is performing very poorly. Significantly,
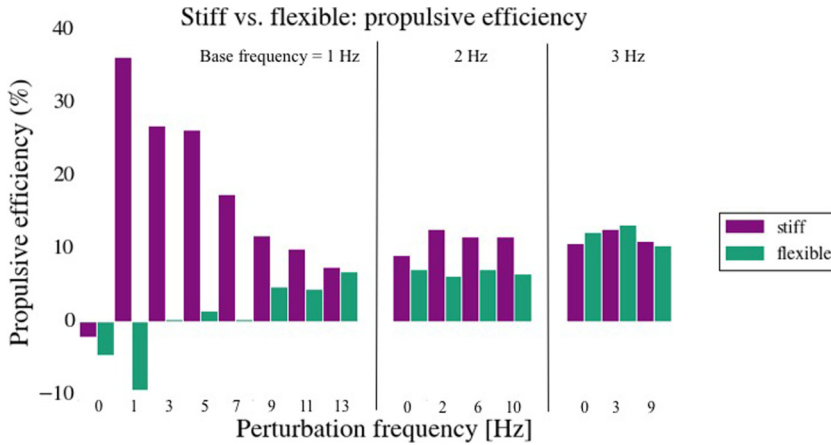
FIG. 6. The propulsive efficiency ($\eta = \frac{F_x V_x}{P}$) is plotted for both the stiffer (purple, $EI = 9.9 \times 10^{-4}$) and flexible (green, $EI = 3.3 \times 10^{-5}$) foils for base frequencies of $f_b = 1$, 2, and 3 Hz and all associated perturbation frequencies.

cases with largely improved performance, such as $f_b = 1$ Hz with a $f_p = 13$ Hz where $C_x = 0.375$, there is a slight increase in propulsive efficiency. Thus, for the flexible foil, the best performing case in the left panel of Fig. 5 is the most efficient on the same panel in Fig. 6.

B. Wake structures

Wake analysis was conducted using PIV to examine the vorticity patterns in the wake for interesting perturbed inputs. The vorticity is shown using a diverging scale of red and blue (all vorticity scales are the same), and the vorticity fields are plotted over the raw images to locate the position of the foil in each frame. All images are taken from instantaneous velocity fields, i.e. no averaging has occurred. In general, for both the stiffer and flexible foils, perturbations increased the intensity of the vorticity and increased the number of individual vortex structures present in the wake.

Flow fields for the stiffer foil with four input functions are shown in Fig. 7. Each input is shown at three phases in the cycle: $T/3$ (left column, the foil is heaving towards the bottom of the frame, its left, as indicated by the yellow arrow), $2T/3$ (center column, and leading edge of the foil has just changed directions), and at the end of the cycle, T (right column, the foil is heaving up). In all cases [Figs. 7(a)–7(d)], the base frequency, $f_b = 1$ Hz. Panel a (top row) shows the vorticity fields when an unperturbed 1 Hz heave is applied to the stiffer foil. While somewhat noisy, the panel generally produces a single vortex each half-cycle (a 2S wake [23]), resulting in a weak reverse von Kármán street. This is an expected result for a heaving panel at this Reynolds number and Strouhal number of 0.1 (defined as $\text{St} = \frac{fA}{U}$, where f is the heave frequency, and A is the trailing edge tip-to-tip amplitude) [10,15]. This is the free swimming case (no net force condition), which can be seen in the location of the vortices in the wake that are lined up, inducing flow directly perpendicular to the incoming velocity.

In Fig. 7(b) (second row), a perturbation with a frequency of $f_p = 3$ Hz has been added to the base signal according to Eq. (1). This results in more individual vortices being shed into the panel's wake, whereas, without the perturbation only same-signed vorticity is shed each half cycle, now both positive and negative vortices enter the wake regardless of the direction of panel motion. The resulting wake is visually similar to a 2P wake [23], but we note that a traditional 2P wake consists of two same-signed vortices being shed each half cycle. In this case, the pair are oppositely signed.

This effect is even more evident for higher perturbation frequencies seen in Fig. 7(c) ($f_p = 7$ Hz) and 7(d) ($f_p = 9$ Hz). While the base frequency alone produces an alternating street of vortices that are largely centered on the spanline of the panel, imposing a high-frequency perturbation [for
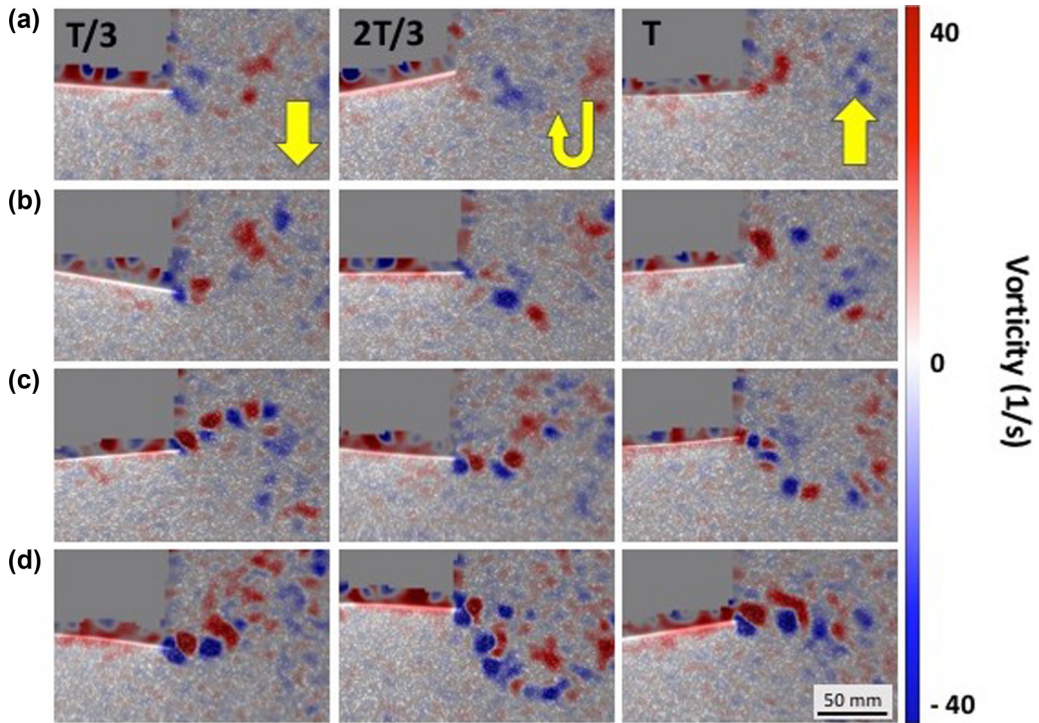
FIG. 7. The ratio of the perturbation frequency to the base frequency alters the wake structure behind the stiffer foil. (a) A base signal (1.0 Hz frequency, 1.0 cm heave amplitude), alone with no perturbation. (b)–(d) The vorticity in the wake for perturbed inputs with perturbation frequencies that are 3 (b), 7 (c), and 9 (d) times the base frequency, respectively. All perturbed inputs have the same base signal and perturbation heave amplitude of 0.1 cm.

example 7 Hz shown in Fig. 7(c)] produces a high-frequency street of smaller, higher intensity vortices that follow the curve of motion of the panel.

Finally, for very high perturbation frequency, $f_p = 9$ Hz [Fig. 7(d)], pairs of oppositely signed vortices are shed from the end of the panel together. The pair remains together as it convects downstream; however, the "street" of vortices seen at lower f_p is less well defined for this case. It is noted that for the stiffer foil with $f_b = 1$ Hz, this perturbation frequency generates the largest forces.

Flow fields for the flexible foil with four input functions are shown in Fig. 8. Once again, each input is shown at three phases in the cycle: $T/3$, $2T/3$, and at the end of the cycle, T. In all cases [Figs. 8(a)–8(d)], the base frequency, $f_b = 1$ Hz, and all contour levels are the same. Figures 8(b)–8(d) show perturbed inputs with perturbation frequencies of $f_p = 17$, 21, and 25 Hz, respectively.

Without a perturbation [Fig. 8(a)], the flexible foil produces very weak vorticity, and the individual structures are hard to distinguish from the noise. It is noted that this case is not force-producing: C_F is negative. However, the addition of perturbations [as seen in Figs. 8(b)–8(d)] greatly increases the intensity of the wake vortices. In addition to stronger vortices, as for the stiffer foil, the perturbations also increase their number. Again, we note that all of the perturbed cases shown are thrust producing with positive C_F of 0.0284, 0.0888, and 0.3567, respectively. As with the high-frequency perturbations in the stiffer case, we see a oppositely signed vortices being shed each half cycle. These follow the motion of the foil in the wake until they begin to break down about 1/2 a chord length downstream of the trailing edge.
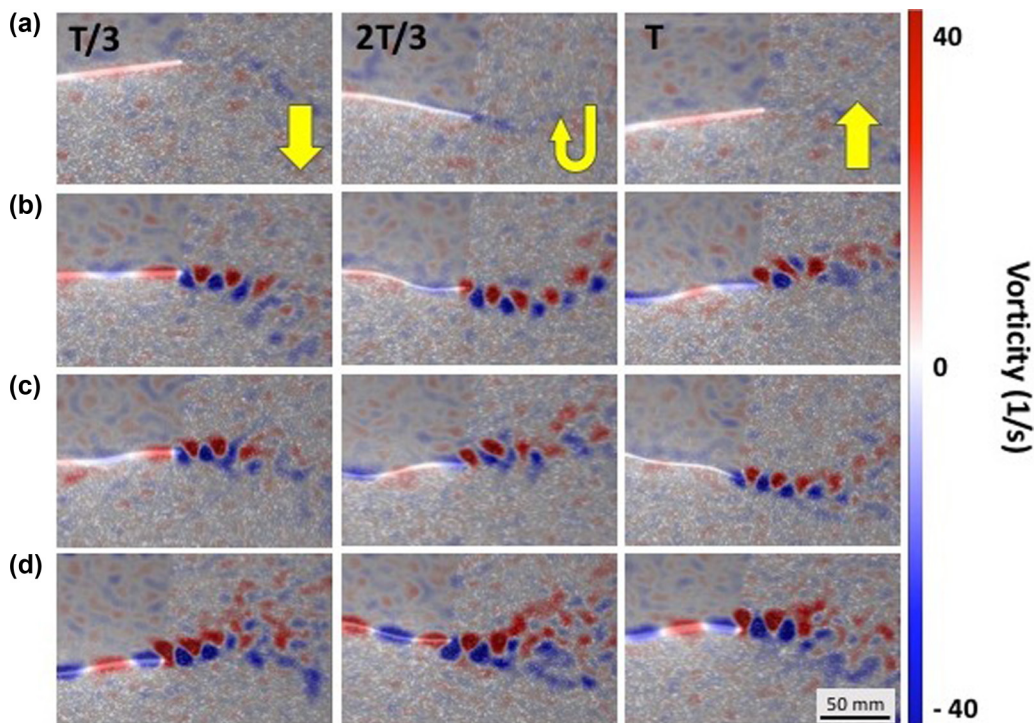
FIG. 8. The ratio of the perturbation frequency to the base frequency alters the wake structure behind the flexible foil. (a) A base signal (0.5 Hz frequency, 1.0 cm heave amplitude), alone with no perturbation. (b)–(d) The vorticity in the wake for perturbed inputs with perturbation frequencies that are 17 (b), 21 (c), and 25 (d) times the base frequency, respectively. All perturbed inputs have the same base signal and perturbation heave amplitude of 0.1 cm.

As f_p increases, the strength of the vorticity *on* the foil also increases. Where in Fig. 8(a), there is a boundary layer of mostly same-signed vorticity attached to the foil, the rest of the panels in Fig. 8, there are regions of both positive and negative vorticity. As f_p increases, those regions become smaller and have higher intensity vorticity. This is reflected in the smaller, higher frequency vortices present in the wake.

C. Velocity profiles

The spanwise velocity profiles for both foils are shown at one downstream location in Fig. 9. The streamwise component of velocity with the incoming flow removed, $(U - V_x)$ is is plotted normalized by V_x. The normalized velocity is plotted against the spanwise position normalized by the span length, y/s. The centerline of the foil is located at $y/s = 0$. The velocity profile is the average velocity calculated over an area immediately downstream of the foil that is 1/6 chord lengths long in the streamwise direction.

For both foils, the data are taken at five instances throughout a single cycle. The input for the stiffer foil, Fig. 9 (left panel), is a base frequency of $f_b = 1$ Hz and a perturbation of $f_p = 7$ Hz. This is the same condition shown in Fig. 7(c). Despite some noise (this is instantaneous data), we see a region of high velocity near the center of the foil with two adjacent regions of reverse flow. Specifically, we note that the location of the spanwise peak moves throughout the cycle. This characteristic is consistent with the flow field shown in Fig. 7(c). The vortex street is not centered on $y/s = 0$, as it typically is for a heaving foil, instead the street meanders throughout the cycle. Thus,
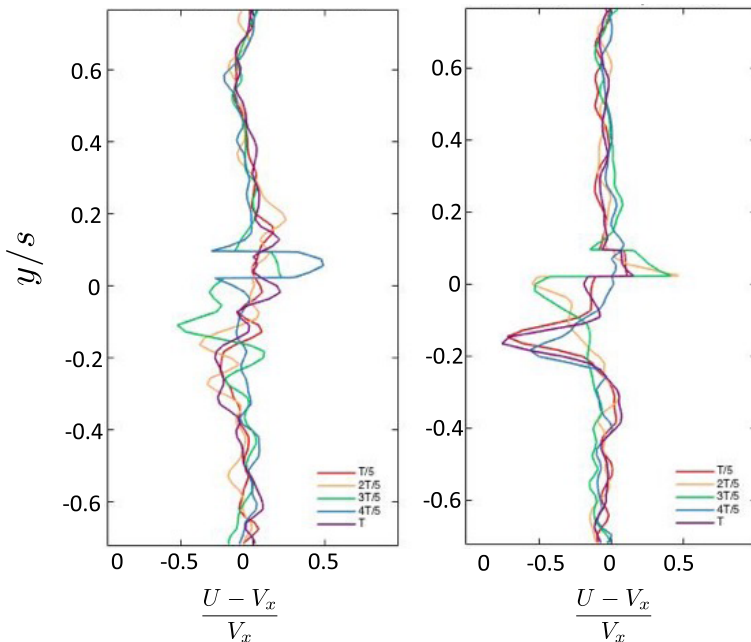
FIG. 9. The streamwise component of velocity ($\frac{U-V_x}{V_x}$) is plotted along the span of the field of view for a streamwise location of 1/6 chords downstream from the end of the foils. Data are taken from instantaneous snapshots of a single heaving cycle at times: 0 (color), $T/5$ (color), $2T/5$ (color), $3T/5$ (color), and $4T/5$ (color). The right panel shows velocity profiles for the stiffer foil with a base frequency of 1 Hz and a 7 Hz perturbation [this flow field is shown in Fig. 7(c)]. The left panel shows the velocity profile for the flexible foil with a base frequency of 0.5 Hz and an 8.5 Hz perturbation [this flow field is shown in Fig. 8(b)].

for perturbed inputs in particular, it can be very useful to look at instantaneous realizations of the flow, as opposed to averages, where these variations can be lost.

IV. DISCUSSION

Fishlike locomotion involves waves of bending that pass down the body from the head toward the tail and generate thrust with a distinctive reverse von Kármán wake hydrodynamic signature. The precise nature of the input signals that swimming fish use to generate these waves of bending is not well understood, although numerous recordings have been made of patterns of electrical activity in the body musculature [35–38]. Two key conclusions from these muscle electrical activity measurements in swimming fish are (1) that there is an alternating pattern of right-left activation and (2) that electrical activity from both sides passes down the body at a speed greater than the traveling mechanical wave.

Muscle electrical activity patterns that drive swimming muscles are produced by neural circuits in the spinal cord and brain stem. Although outputs from these circuits appear to produce relatively smoothly time-varying movements, there is increasing evidence that output signals from the nervous system controlling motor behaviors represent a combination of a smooth base signal with the addition of other oscillatory inputs that introduce variation [39]. Circuits that add variation to output signals may be common in neural control systems that are involved in regulating behaviors such as swimming.

Although there have been many recent studies that use simple physical models to understand the hydrodynamics of aquatic propulsion [10,15,24,32,33,40], all of these have employed smooth sinusoidal or sawtooth-like input waves to drive the leading edge of passive swimming panels. In

this study our aim has been to extend this line of research to include a higher frequency modulatory signal driving panels with relatively high (fishlike) flexibility, inspired by recent analyses of neural circuits that control motor behavior, which demonstrate the existence of variable inputs to a base control output signal.

The two foil stiffnesses studied here were chosen specifically to allow comparison to previous studies of flapping propulsion using highly flexible foils [31], and to correspond to the range of measured stiffnesses on the bodies of live fishes. Although measurements of fish body flexural stiffness are limited and there is considerable variation along the body, the estimates that are available range from about 1×10^{-3} Nm^2 near the head to 1×10^{-6} Nm^2 near the tail [31,41,42]. Propulsion driven by a heave motion at the leading edge in these highly flexible foils displays kinematics and wake structures that correspond well to that of the propulsive regions of live fishes, and there are a number of reasons to believe that such passive foils are a good model for flexible fishlike swimming [8,31]. For example, at slow to moderate swimming speeds, fish use only about 2%–5% of their body muscle mass to power body bending and the body functions largely as a passively flexing foil. We thus believe that data from analyses of flexible foils with similar flexural stiffness to that of fish bodies are able to provide insights into the dynamics of aquatic propulsion in fishes, and to inspire future biological measurements on freely swimming fishes.

Our most significant overall result is that applying high-frequency, low-amplitude perturbations to a sinusoidal heaving foil will generally increase both the propulsive output of the foil over the force generated by a heaving foil alone and the efficiency of propulsion, and sometimes dramatically so. It appears that this occurs because the perturbation reorganizes boundary layer vorticity along the foil such that stronger, more frequent vortices can be shed into the foil's wake. Perturbations cause the transition from a 2S to 2P wake, then finally an alternating street of vortices that follows the base heaving motion of the panel through the wake. This is significantly different than results for nonperturbed heaving panels. While sometimes, for highly flexible propulsors, the boundary layer fails to roll up into distinct vortices and a shear layer is shed into the wake more or less following the motion of the leading edge [15,34], there are not distinct, strong vortices in these cases. Furthermore, they tend to produce very little forward force (or even generate net negative streamwise force, drag). However, in addition to the wake structure shown here by swimming foils when perturbations are added, we often see significant force augmentation with the addition of the high-frequency perturbation.

From Fig. 4 (left panel), it is clear that a peak in performance occurs for the stiffer foil when a perturbation of 9 Hz is applied to the base heave signal. This is true up to a base frequency of 1.75 Hz (above this, we do not have sufficiently resolved data to identify the presence or absence of a peak). While a clear peak is not visible in Fig. 4 for the flexible foil (right panel), we still see an increasing trend in the force production at perturbations of 13 Hz. It is possible that the peak exists, but at higher perturbation frequencies than we can reach with the current experimental apparatus. There is a small peak evident at the two lowest base frequencies when a perturbation of 9 Hz is added, but the relative increase in force production is small compared to that observed for the stiffer foil, and this peak is not evident at higher base frequencies. Furthermore, this increase in streamwise force does not always come at a cost to efficiency. In fact, some high-performance cases, for example, the stiffer foil with $f_b = 1$ Hz and a $f_p = 9$ Hz perturbation, also have a high propulsive efficiency.

The stiffer foil experiences much more dramatic changes in both force production and efficiency as perturbations are added compared to the flexible foil (Figs. 5 and 6). For the stiffer foil there appears to be a relatively broad range of perturbation frequencies that greatly improve propulsive efficiency. This suggests that adding almost any perturbation in the 2–8 Hz range is sufficient to introduce changes in flow around the foil greatly increasing propulsive efficiency, and that these increases in efficiency are relatively insensitive to specific perturbation frequencies. In contrast, while propulsive efficiency of the flexible foil is generally improved by the addition of perturbation frequencies, the factorial increase is much less than for the stiffer foil.

In an attempt to understand the physical origin of these results, and to determine if there is optimal perturbation size for a given foil stiffness and/or size, scaling laws for both the elastic and hydrodynamic forces have been explored. Quinn *et al.* defined as the effective flexibility $\Pi_1 =$

$(\rho s f^2 L^5/EI)^{1/2}$, which is the ratio of added mass to bending forces [15]. However, while very enlightening for smoothly heaving foils of varying flexibility, it does not allow us to account for the perturbation frequency, f_p. Using traditional scaling, such as the ratio of perturbation to base frequencies, f_p/f_b, the peak in C_f is no longer at a constant location. It occurs at increasingly lower ratios of f_p/f_b for higher base heave frequencies. Thus, with experimental data, we are not able to investigate the hydrodynamic forces compared to the bending forces with respect to the perturbation bending in such a way as to provide an optimal value of the perturbation-rigidity size. Graphs provided as Supplemental Material [43] illustrate the relationships between this elastic force coefficient and the dimensionless frequency ratio f_p/f_b, and between the force coefficient and this ratio. Further exploration of this using an analytical approach, which can investigate a wider parameter space, could hopefully lead to this type of insight.

Under a number of biological conditions efficiency is not always the best criterion to judge animal performance, as alternative metrics such as peak thrust may be of primary importance in behaviors such as escape from predators. However, it is noteworthy that adding a higher frequency perturbation to the base frequency (especially for the stiffer foil) greatly increased both force production and efficiency. This suggests the interesting possibility that adding higher frequency perturbations to base control signals may enable flexible flapping propulsive systems to avoid or at least minimize the tradeoff between speed and efficiency and achieve relatively high values of both under conditions which would not be possible without the use of a more complex control signal. These data suggest that future engineering analyses of flapping propulsive systems utilizing fishlike flexible foils might benefit from examining a broader range of input parameters than have traditionally been studied. Correspondingly, biological analyses of aquatic propulsion might profitably focus on the nature of the control signals generated by the nervous system to determine if swimming fishes use higher frequency modulations of a base signal to increase locomotor performance.

V. CONCLUSIONS

For both a stiffer and a highly flexible foil, the addition of a high-frequency, low amplitude sinusoidal perturbation to a standard sinusoidal base signal increases the streamwise force production of the foil in almost all cases. While this is sometimes at a small cost in efficiency, there are cases where the perturbation results in dramatic increases in efficiency. Furthermore, for the stiffer foil, a peak in force production occurs for a perturbation frequency between 8 and 9 Hz, regardless of the base heave frequency.

The addition of perturbations causes, first, a transition from a 2S to a 2P wake structure in the stiffer foil [23]. Further increasing the frequency of the perturbation increases both the intensity of the vorticity and the vortex shedding frequency, above two pairs per cycle. While less easily categorized, the same trend is seen for the flexible foil, with the addition of alternate signed, high-intensity vorticity becoming apparent along the foil.

ACKNOWLEDGMENTS

[1] M. J. Lighthill, Aquatic animal propulsion of high hydromechanical efficiency, J. Fluid Mech. **44**, 265 (1970).

[2] M. J. Lighthill, Large-amplitude elongated-body theory of fish locomotion, Proc. R. Soc. London B **179**, 125 (1971).

[3] P. W. Webb, Hydrodynamics and energetics of fish propulsion, Bull. Fisheries Res. Board Canada **190**, 1 (1975).

[4] G. V. Lauder, E. J. Anderson, J. Tangorra, and P. G. A. Madden, Fish biorobotics: Kinematics and hydrodynamics of self-propulsion, J. Exp. Biol. **210**, 2767 (2007).

[5] R. W. Blake, *Fish Locomotion* (Cambridge University Press, Cambridge, 1983).

[6] G.V. Lauder and E. D. Tytell, Hydrodynamics of undulatory propulsion, in *Fish Biomechanics*, edited by R. E. Shadwick and G. V. Lauder (Academic Press, San Diego, 2006), pp. 425–468.

[7] M. S. Triantafyllou, G. S. Triantafyllou, and D. K. P. Yue, Hydrodynamics of fishlike swimming, Annu. Rev. Fluid Mech. **32**, 33 (2000).

[8] E. D. Tytell, M. C. Leftwich, C.-Y. Hsu, B. E. Griffith, A. H. Cohen, A. J. Smits, C. Hamlet, and L. J. Fauci, Role of body stiffness in undulatory swimming: Insights from robotic and computational models, Phys. Rev. Fluids **1**, 073202 (2016).

[9] J. H. J. Buchholz and A. J. Smits, Wake of a low aspect ratio pitching plate. Phys. Fluids **17**, 091102 (2005).

[10] J. H. Buchholz and A. J. Smits, On the evolution of the wake structure produced by a low aspect ratio pitching panel, J. Fluid Mech. **546**, 433 (2006).

[11] M. A. Green, Analysis of bio-inspired propulsors, Ph.D. thesis, Princeton University, Princeton, NJ (2009).

[12] M. S. Triantafyllou, A. H. Trachet, and F. S. Hower, Review of experimental work in biomimetic foils, IEEE J. Ocean. Eng. **29**, 585 (2004).

[13] J. H. Buchholz and A. J. Smits, The wake structure and thrust performance of a rigid low-aspect-ratio pitching panel, J. Fluid Mech. **603**, 331 (2008).

[14] M. A. Green, C. W. Rowley, and A. J. Smits, The unsteady three-dimensional wake produced by a trapezoidal pitching panel, J. Fluid Mech. **685**, 117 (2011).

[15] D. B. Quinn, G. V. Lauder, and A. J. Smits, Flexible propulsors in ground effect, Bioinspiration Biomimetics **9**, 036008 (2014).

[16] H. Dong, M. Bozkurttas, R. Mittal, P. Madden, and G. V. Lauder, Computational modeling and analysis of the hydrodynamics of a highly deformable fish pectoral fin, J. Fluid Mech. **645**, 345 (2010).

[17] R. Root, H.-W. Courtland, W. Shepherd, and J. Long, Flapping flexible fish, Exp. Fluids **43**, 779 (2007).

[18] R. G. Root and C. W. Liew, Computational and mathematical modeling of the effects of tailbeat frequency and flexural stiffness in swimming fish, Zoology **117**, 81 (2014).

[19] J. M. Camhi, *Neuroethology: Nerve Cells and the Natural Behavior of Animals* (Sinauer Associates, Sunderland, MA, 1984).

[20] J. Buchanan, Neural control of locomotion in lower vertebrates: From behavior to ionic mechanisms, in *Neural Control of Rhythmic Movements in Vertebrates*, edited by A. H. Cohen, S. Rossignol, and S. Grillner (Wiley, New York, 1988), pp. 1–40.

[21] K. G. Pearson, Common principles of motor control in vertebrates and invertebrates, Annu. Rev. Neurosci. **16**, 265 (1993).

[22] K. G. Pearson, Generating the walking gait: Role of sensory feedback, Prog. Brain Res. **143**, 123 (2004).

[23] C. H. K. Williamson and A. Roshko, Vortex formation in the wake of an oscillating cylinder, J. Fluids Structures **2**, 355 (1988).

[24] F. S. Hover, O. Haugsdal, and M. S. Triantafyllou, Effect of angle of attack profiles in flapping foil propulsion, J. Fluids Structures **19**, 37 (2004).

[25] S. C. Licht, M. S. Wibawa, F. S. Hover, and M. S. Triantafyllou, In-line motion causes high thrust and efficiency in flapping foils that use power downstroke, J. Exp. Biol. **213**, 63 (2010).

[26] M. Kaya and I. H. Tuncer, Nonsinusoidal path optimization of a flapping airfoil, AIAA J. **45**, 2075 (2007).

[27] K. Lu, Y. H. Xie, and D. Zhang, Numerical study of large amplitude, nonsinusoidal motion and camber effects on pitching airfoil propulsion, J. Fluids Structures **36**, 184 (2013).

[28] E. Mollerstedt and B. Bernhardsson, Out of control because of harmonics-an analysis of the harmonic response of an inverter locomotive, IEEE Control Syst. **20**, 70 (2000).
[29] D. B. Quinn, G. V. Lauder, and A. J. Smits, Scaling the propulsive performance of heaving flexible panels, J. Fluid Mech. **738**, 250 (2014).
[30] D. B. Quinn, G. V. Lauder, and A. J. Smits, Maximizing the efficiency of a flexible propulsor using experimental optimization, J. Fluid Mech. **767**, 430 (2015).
[31] R. M. Shelton, P. J. M. Thornycroft, and G. V. Lauder, Undulatory locomotion of flexible foils as biomimetic models for understanding fish propulsion, J. Exp. Biol. **217**, 2110 (2014).
[32] K. N. Lucas, P. J. M. Thornycroft, B. J. Gemmell, S. P. Colin, J. H. Costello, and G. V. Lauder, Effects of non-uniform stiffness on the swimming performance of a passively-flexing, fish-like foil model, Bioinspiration Biomimetics **10**, 056019 (2015).
[33] D. A. Read, F. S. Hover, and M. S. Triantafyllou, Forces on oscillating foils for propulsion and maneuvering, J. Fluids Structures **17**, 163 (2003).
[34] M. C. Leftwich, E. D. Tytell, A. H. Cohen, and A. J. Smits, Wake structures behind a swimming robotic lamprey with a passively flexible tail, J. Exp. Biol. **215**, 416 (2012).
[35] J. D. Altringham, C. S. Wardle, and C. I. Smith, Myotomal muscle function at different locations in the body of a swimming fish, J. Exp. Biol. **182**, 191 (1993).
[36] B. Jayne and G. Lauder, Red muscle motor patterns during steady swimming in largemouth bass: Effects of speed and correlations with axial kinematics, J. Exp. Biol. **198**, 1575 (1995).
[37] L. C. Rome, P. T. Loughna, and G. Goldspink, Muscle fiber activity in carp as a function of swimming speed and muscle temperature, Am. J. Phys. **247**, R272 (1984).
[38] C. S. Wardle and J. J. Videler, The timing of the electromyogram in the lateral myotomes of mackerel and saithe at different swimming speeds, J. Fish Biol. **42**, 347 (1993).
[39] H. G. Wu, Y. R. Miyamoto, L. N. Gonzalez Castro, B. P. Ölveczky, and M. A. Smith, Temporal structure of motor variability is dynamically regulated and predicts motor learning ability, Nat. Neurosci. **17**, 312 (2014).
[40] F. Paraz, L. Schouveiler, and C. Eloy, Thrust generation by a heaving flexible foil: Resonance, nonlinearities, and optimality, Phys. Fluids **28**, 011903 (2016).
[41] M. J. McHenry, C. A. Pell, and J. H. Long, Mechanical control of swimming speed: Stiffness and axial wave form in undulating fish models, J. Exp. Biol. **198**, 2293 (1995).
[42] J. H. Long, Muscles, elastic energy, and the dynamics of body stiffness in swimming eels, Am. Zool. **38**, 771 (1998).
[43] See Supplemental Material at http://link.aps.org/supplemental/10.1103/PhysRevFluids.2.023101 for the axial coefficient of force as a function of the ratio of the perturbation frequency to the base frequency (Fig. S1), and the axial coefficient of force as a function of the ratio of the perturbation frequency to the base frequency times the hydrodynamics coefficient of force (Fig. S2). Both of these plots, and Fig. 4, contain the same data presented in different manners.